Supplementary Information (SI) for Chemical Science.
This journal is © The Royal Society of Chemistry 2026

Electronic Supplementary Information

Constructing Interfacial Charge Transfer Channels via Plasmon-Mediated Dual Excitation in S-Vacancy-Rich $ZnIn_2S_4$/CuSe Heterostructures for Enhanced NIR-Driven H_2 Production

Yuanyong Huang,[‡a] Cai Ning,[‡a] Xinyu Lu,[a] Yang Chao,[a] Junhao He,[a] Qiankun Gao,[a] Yu Yu,[a] Zhongkai Xie,[a] Hailing Huo,[a] and Weidong Shi[*a,b]

[a] College of Environmental and Chemical Engineering, Jiangsu University of Science and Technology, Zhenjiang, 212003, P.R. China.

[b] School of Chemistry and Chemical Engineering, Jiangsu University, Zhenjiang, 212013, P.R. China

[‡] Y. Huang and C. Ning contributed equally to this work.

* Corresponding email: swd1978@ujs.edu.cn

Experimental section.

1.1. Materials

All chemical reagents used in the experiments were purchased and used without further purification, unless otherwise specified. The $CuCl_2 \cdot 2H_2O$, NaOH, TiO_2, Na_2SO_4, NaCl, HCl, anhydrous ethanol (C_2H_5OH), $C_4H_6O_4Zn \cdot 2H_2O$, $BaSO_4$, triethanolamine (TEOA: $C_6H_{15}NO_3$) and urea ($CO(NH_2)_2$) were purchased from Sinopharm Chemical Reagent Co., Ltd. (China). The polyvinyl pyrrolidone (PVP: $(C_6H_9NO)_n$) was obtained from Bidepharm (Shanghai, China). $InCl_3$ and thioacetamide (TAA: C_2H_5NS) were purchased from Aladdin Chemistry Co. Ltd. (China). Selenium powder (Se) was obtained from Shanghai Macklin Biochemical Co. Ltd. China.

1.2. Synthesis of g-C_3N_4

The as-obtained sample was collected for further characterization after naturally cooling to room temperature. Typically, 10.0 g of urea is finely ground in a mortar, transferred to a 50 mL crucible, and heated at 550 °C for 3 hours in an air atmosphere.

1.3. Synthesis of CuSe

Firstly, a 1.0 mol/L NaOH solution was prepared by dissolving 2.0 g of NaOH in 50 mL of ultrapure water. The solution was then cooled to room temperature, and 5 mmol of $CuCl_2 \cdot 2H_2O$ was added and stirred for 10 minutes. Next, 150 mg of PVP was added, and the mixture was stirred for 30 minutes. Subsequently, 2 mmol of Se powder was introduced into the solution and stirred for another 30 minutes. The resulting mixture was transferred to a 100 mL reactor and heated at 120 °C for 24 hours. After cooling to room temperature, the black precipitate was collected, washed several times by centrifugation with ultrapure water and anhydrous ethanol, and then dried in a vacuum oven at 60 °C overnight.

1.4. Synthesis of NIR-responsive $ZnIn_2S_4$ with sulfur vacancies (Vs-$ZnIn_2S_4$)

Similar to the methods previously reported in the literature,[1] 0.8 mmol of $C_4H_6O_4Zn \cdot 2H_2O$, 1.6 mmol of $InCl_3$, and 6.4 mmol of C_2H_5NS were weighed and dissolved in 30 mL of ultrapure water and 30 mL of anhydrous ethanol, then stirred for 30 minutes. The solution was transferred to a 100 mL reactor and heated at 180 °C for 24 hours. After cooling to room temperature, the resulting yellow precipitate was washed repeatedly by centrifugation with ultrapure water and anhydrous ethanol, and then dried in a vacuum oven at 60 °C overnight. The pure $ZnIn_2S_4$ sample was labeled as ZIS.

1.5. Synthesis of CuSe@Vs-$ZnIn_2S_4$, CuSe@g-C_3N_4 and CuSe@TiO_2 nanohybrid

In a typical procedure, 1 g of as-prepared $ZnIn_2S_4$ and varying amounts of CuSe (5, 10, and 20 mg) were weighed and added to 30 mL of ultrapure water and 30 mL of anhydrous ethanol, then stirred for 30 minutes. The mixture was transferred to a 100 mL reactor and heated at 120 °C for 24 hours. After cooling to room temperature, the resulting precipitates were washed repeatedly by centrifugation with ultrapure water and anhydrous ethanol, and then dried in a vacuum oven at 60 °C overnight. The resulting solid powders were labeled as $Z@Cu_{(0.5wt\%)}$, $Z@Cu_{(1wt\%)}$, and $Z@Cu_{(2wt\%)}$, respectively. For comparison, CuSe@g-C_3N_4 and CuSe@TiO_2 nanohybrids were also prepared using a similar procedure. Specifically, 1 g of as-prepared g-C_3N_4 and 1 g of TiO_2 were each combined with 10 mg of CuSe, then added to 30 mL of ultrapure water and 30 mL of anhydrous ethanol, and stirred for 30 minutes. The mixtures were then transferred to a 100 mL reactor and heated at 120 °C for 24 hours. After cooling to room temperature, the resulting precipitates were washed repeatedly by centrifugation with ultrapure water and anhydrous ethanol, and then dried in a vacuum oven at 60 °C overnight.

1.6. Characterizations.

Powder X-ray diffraction (PXRD) patterns were carried out by a DX2700BH with Cu-Kα_1 radiation (λ = 1.5406 Å) (Haoyuan Instrument, China) (Fig. S1). The Cu:Se ratio was measured using Inductively Coupled Plasma Optical Emission Spectroscopy (ICP-OES) (Model 720, Agilent Technologies, USA). Scanning electron microscopy (SEM) was performed to observe the microstructure of the catalysts by a S-4800 (Hitachi, Japan). Transmission electron microscopy (TEM) was analyzed by a FEI TALOS 200X (Thermo Fisher, America). Atomic force microscope (AFM) was tested by a Dimension Icon (Bruker, Germany). X-ray photoelectron spectra (XPS) spectra were obtained by a ESCALAB 250Xi (Thermo Scientific, United States). Electron paramagnetic resonance (EPR) measurements were carried out by an EMXplus-6/1 (Bruker, Germany). The UV-visible-NIR diffuse reflectance spectra (UV-Vis-NIR DRS) were collected by a Shimadzu UV-2450 spectrophotometer (Japan). Steady-state PL spectroscopy was performed on an Edinburgh FLS980 spectrometer.

1.7. Photoelectrochemical measurements

The photoelectrochemical properties of the catalysts were analyzed using an electrochemical workstation (CHI-760E). A traditional three-electrode system was employed, consisting of a 0.5 M Na_2SO_4 electrolyte solution (pH 6.8), a working electrode (prepared sample), a Pt sheet as the counter electrode, and an Ag/AgCl electrode as the reference electrode. For the preparation of the working electrode, 10 mg of photocatalyst was first added in 3 mL of ethanol, mixed with 50 μL of Nafion, and then applied to a 0.5 cm × 1 cm FTO substrate. The coated electrode was dried at room temperature. Finally, the photocurrent behavior of the catalysts was analyzed at wavelengths

greater than 800 nm. We performed electrochemical impedance spectroscopy (EIS) over a frequency range of 10^{-2} to 10^{6} Hz.

1.8. Electron paramagnetic resonance (EPR) measurements

The solid samples were ultrasonically dispersed in the corresponding solvent to prepare a 1 mg/mL solution. Then, 30 μL of the sample solution was taken, mixed with 30 μL of DMPO as the trapping agent and 100 mM methanol as the solvent. After thoroughly mixing, a certain amount of the mixture was drawn into a capillary tube, which was then placed inside a quartz tube and positioned in the EPR sample cavity. The instrument parameters were set as follows: center field: 3499 G, sweep width: 100.0 G, power: 6.325 mW, microwave attenuation: 15.0 dB, resonance frequency: 9.824131 GHz, sweep time: 30.00 s, modulation amplitude: 1.000 G, and modulation frequency: 100.00 kHz. Finally, the prepared sample solution was irradiated in situ with NIR light at a wavelength greater than 800 nm for 5 minutes.

1.9. Transient absorption measurements

Transient absorption measurements were conducted under ambient conditions using a Helios pump–probe system (Ultrafast Systems LLC) coupled with an amplified femtosecond laser system (Coherent). The 400 nm pump pulses (~0.5 μJ/pulse at the sample) were provided by an optical parametric amplifier (TOPAS-800-fs), which was excited by a Ti:sapphire regenerative amplifier (Legend Elite-1K-HE; 800 nm, 35 fs, 7 mJ/pulse, 1 kHz), seeded by a mode-locked Ti:sapphire laser system (Micra 5) and pumped by a Nd:YLF laser (Evolution 30). White-light continuum (WLC) probe pulses (820–1400 nm) were generated by focusing the 400 nm beam (split from the regenerative amplifier with a small portion, ~400 nJ/pulse) onto a sapphire plate. A reference beam, split from the WLC, was used to correct pulse-to-pulse fluctuations in the WLC. The time delay (0–8 ns) between the pump and probe pulses was varied using a motorized optical delay line. The instrument response function (IRF) was determined to be approximately 120 fs through a standard cross-correlation procedure. A mechanical chopper operating at 500 Hz modulated the pump pulses, allowing for the alternate recording of transient absorption spectra with and without the pump pulses. The temporal and spectral profiles (chirp-corrected) of the pump-induced differential transmission of the WLC probe light (i.e., absorbance changes) were captured using an optical fiber-coupled multichannel spectrometer equipped with a CMOS sensor. Measurements were performed with the pump and probe polarizations oriented at the magic angle relative to the sample. To obtain reliable data and achieve the high signal-to-noise ratios required for global analysis, at least five scans were acquired and averaged, depending on the signal amplitude in the femtosecond NIR transient absorption measurements.

1.10. Theoretical calculation

Spin-polarized density functional theory (DFT) calculations were performed using the Vienna Ab-initio Simulation Package (VASP) with the projector-augmented wave (PAW) method to describe core-electron interactions.[2] The Perdew-Burke-Ernzerhof (PBE) exchange-correlation functional within the generalized gradient approximation (GGA) was employed.[3] An energy cutoff of 400 eV was applied for the plane-wave basis set. Van der Waals interactions were included using the DFT-D3 method of Grimme.[4] The Brillouin zone was sampled using a 2 × 2 × 1 k-point grid. The structural optimization was conducted with an energy convergence criterion of 1×10^{-5} eV and a force convergence criterion of -0.02 eV/Å. For electronic structure calculations, the energy convergence criterion was 1×10^{-6} eV, and the force convergence criterion was -0.01 eV/atom. A vacuum layer of 15 Å was added to the slab models along the *z*-direction to eliminate spurious interactions between periodic images. In the Slab model, during the optimization process, the two bottom layers are held fixed, while the remaining layers are allowed to relax and undergo structural optimization. The slab model for CuSe was based on the (006) crystallographic plane with a unit cell lattice constant of 4.02 × 4.02 Å. The Vs-$ZnIn_2S_4$ (sulfur vacancy) slab model was constructed using the (102) crystallographic plane, with a unit cell lattice constant of 6.79 × 3.92 Å, consistent with experimental results. The heterostructure was constructed by identifying the minimum energy configuration along the *x*, *y*, and *z* directions to obtain the initial structure. The final heterostructure's lattice parameters were optimized to 28.73 × 7.8496 × 35.000 Å. The lattice mismatch between the heterostructure components was controlled to be less than 3%, ensuring structural compatibility and stability. The binding energy (E_b) of the heterostructure was calculated as:

$$E_b = E_{hetero} - (E_{slab1} + E_{slab2}) \quad (1)$$

where E_{hetero} is the total energy of the heterostructure, E_{slab1} and E_{slab2} are the energies of the individual slabs. A more negative E_b indicates stronger binding and better stability of the heterostructure.

Charge transfer and bonding characteristics were analyzed using Bader charge analysis and charge density difference plots.[5] The spin-polarized DFT calculations were performed in the Device Studio-integrated Projector Augmented-Wave method package (DS-PAW), with the aid of DS-PAW for calculating the projected density of states (PDOS), Bader charge transfer, and charge density difference.[6] Projected density of states (PDOS) calculations were performed to explore the electronic structure.

Gibbs free energy changes (ΔG) were calculated to evaluate the catalytic properties and stability of the system. The Gibbs free energy was expressed as:

$$\Delta G = \Delta E + \Delta ZPE - T\Delta S \quad (2)$$

where ΔE is the adsorption energy obtained from DFT calculations, ΔZPE is the change in zero-point energy, T is the temperature (set to 298.15 K), and ΔS is the entropy change.

1.11. Photocatalytic activity evaluation

The NIR-driven water splitting for H_2 production was evaluated in a closed photoreactor, coupled with an online analysis system using a LabSolar 6A (Beijing Perfectlight Co., Ltd.). First, 20 mg of photocatalyst was weighed, and 40 mL of ultrapure water and 10 mL of triethanolamine (TEOA) were added as a sacrificial agent. The reaction solution was then sonicated for 5 minutes to ensure the photocatalyst was uniformly dispersed. Next, the reaction system was evacuated several times with a vacuum pump, and the temperature of the reaction solution was maintained at 20 °C throughout the experiment using a circulating water pump. The reactor was then irradiated with NIR light from a 300 W xenon lamp, equipped with an 800 nm cut-off filter ($\lambda > 800$ nm). The evolved gas products were analyzed using an online gas chromatography system with a thermal conductivity detector (TCD), fitted with a 5 Å molecular sieve column, and high-purity argon (99.999%) was used as the carrier gas.

Additionally, the apparent quantum yield (AQY) of the CuSe@$ZnIn_2S_4$ composite photocatalyst was calculated under illumination from a 300 W xenon lamp equipped with a monochromator at $\lambda = 940$ nm, with reference to previously reported method. The light intensity was recorded to be 0.38 $mW \cdot cm^{-2}$ by a spectroradiometer and the irradiation area was 12.56 cm^2. The amount of H_2 molecule yielded at 3 h was 6.55 μmol. The AQY was calculated using the following equations:

$$\text{AQE} = \frac{N_e}{N_p} \times 100\% = \frac{2 \times n_{H_2} \times N_A \times h \times c}{S \times P \times t \times \lambda} \times 100\% \qquad (3)$$

where where P, S, λ, h and c are the light-irradiated intensity, the illumination area, the wavelength of the incident light, the Planck constant and the velocity of light, respectively.

1.12. Photocatalytic stability evaluation

In line with the photocatalytic activity evaluation procedure, the best photocatalysts selected were subjected to continuous NIR light irradiation ($\lambda > 800$ nm) to assess their stability in long-term photocatalytic reactions. Next, the reusability of the samples was evaluated. After 9 hours of NIR light exposure, the light source was turned off, and the system was evacuated for 30 minutes before retesting the performance. Multiple cycles of this process were carried out to evaluate the stability of the catalyst during repeated use. Then, the catalyst stability under continuous NIR light irradiation in high-acid (pH = 1), high-alkaline (pH = 12), and high-salt (5 M NaCl) conditions was assessed to evaluate its long-term effectiveness and reliability in practical applications. Finally, after centrifugally drying the tested catalysts, their XRD patterns were measured and compared with the XRD results obtained before and after cycling to analyze the structural stability of the catalyst using a smartlab9 (Rigku, Japan) (Fig. S8).

Supplementary Figures

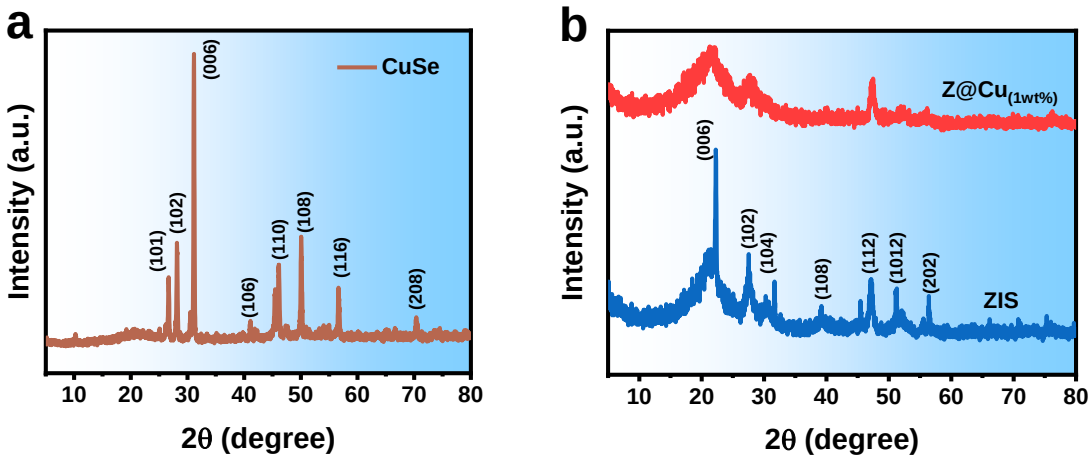

Fig. S1. The XRD patterns of CuSe nanosheets, Vs-$ZnIn_2S_4$ and their composite samples.

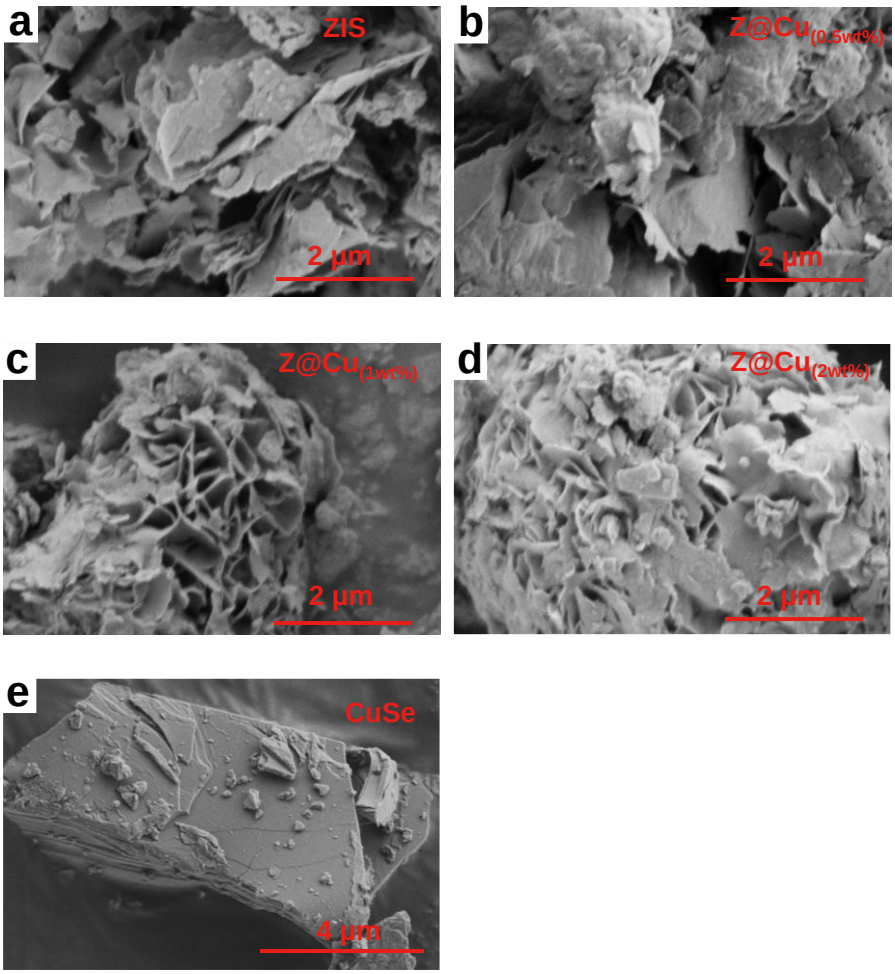

Fig. S2. SEM images of as-prepared Vs-$ZnIn_2S_4$, CuSe and their composites.

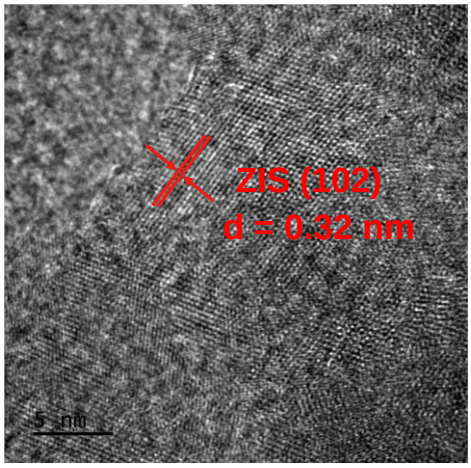

Fig. S3. Representative HRTEM images of $ZnIn_2S_4$.

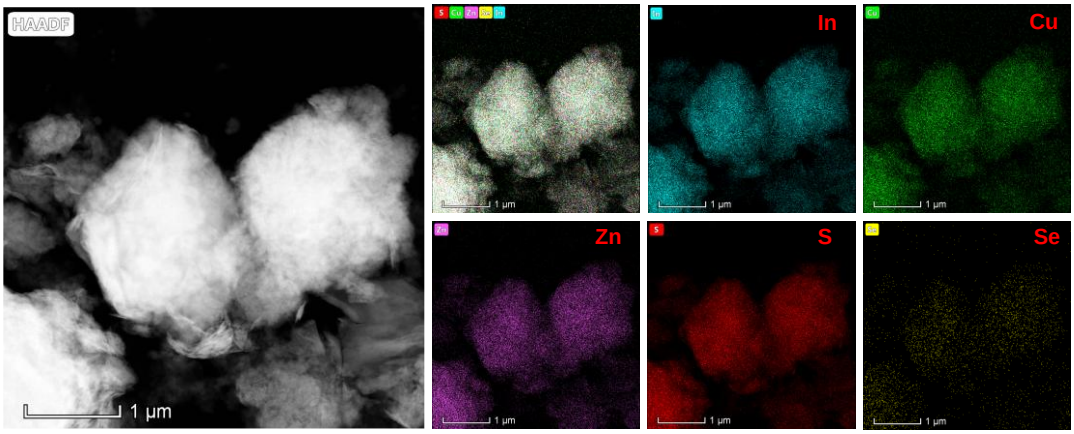

Fig. S4. HAADF-STEM and EDX elemental mapping images of Zn, In, S, Cu, and Se in Vs-$ZnIn_2S_4$@CuSe. Scale bar: 1 µm.

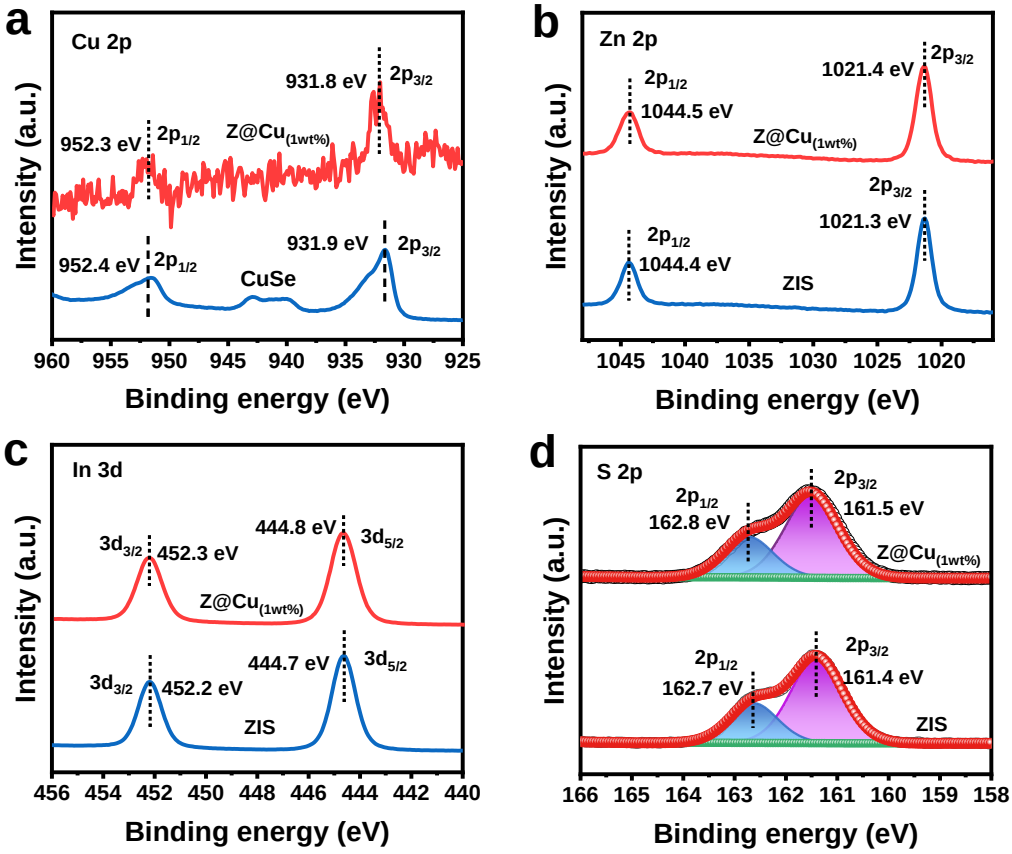

Fig. S5. XPS spectra of CuSe, Vs-$ZnIn_2S_4$ and Vs-$ZnIn_2S_4$@CuSe. (a) Cu 2p orbitals; (b) Zn 2p orbitals; (c) In 3d orbitals; (d) S 2p in Vs-$ZnIn_2S_4$ sheets and Z@$Cu_{(1wt\%)}$.

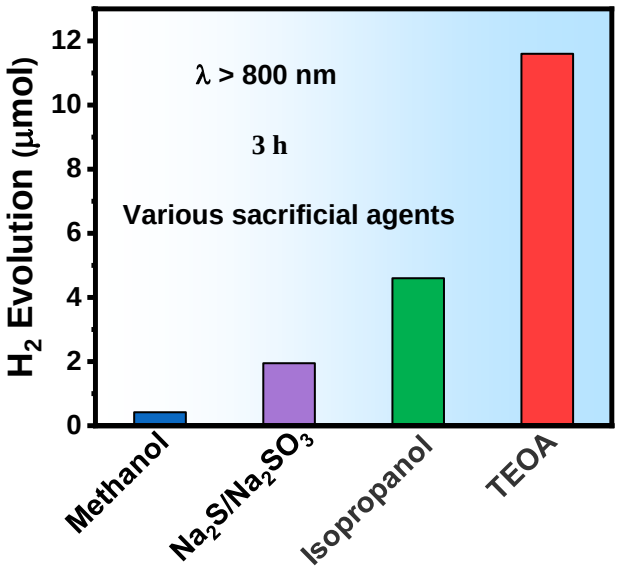

Fig. S6. H_2 production performance in water splitting with different sacrificial agents under NIR light irradiation for 3 hours.

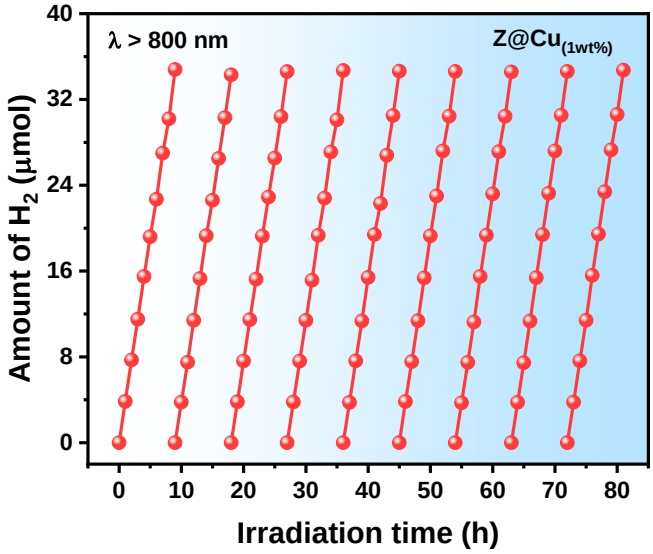

Fig. S7. Cycling stability test of H_2 production performance under NIR light irradiation conditions.

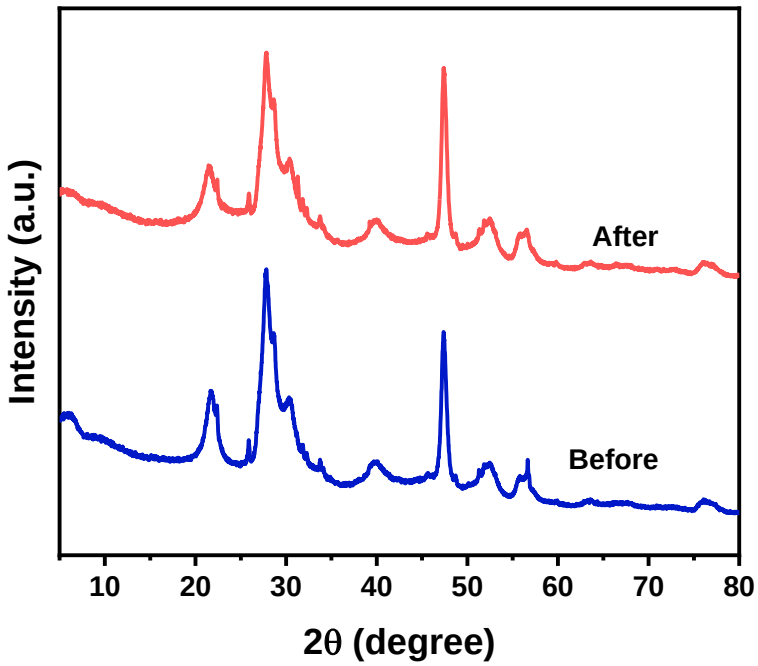

Fig. S8. The XRD patterns of $Z@Cu_{(1wt\%)}$ sample before and after cycling under NIR light irradiation (λ > 800 nm).

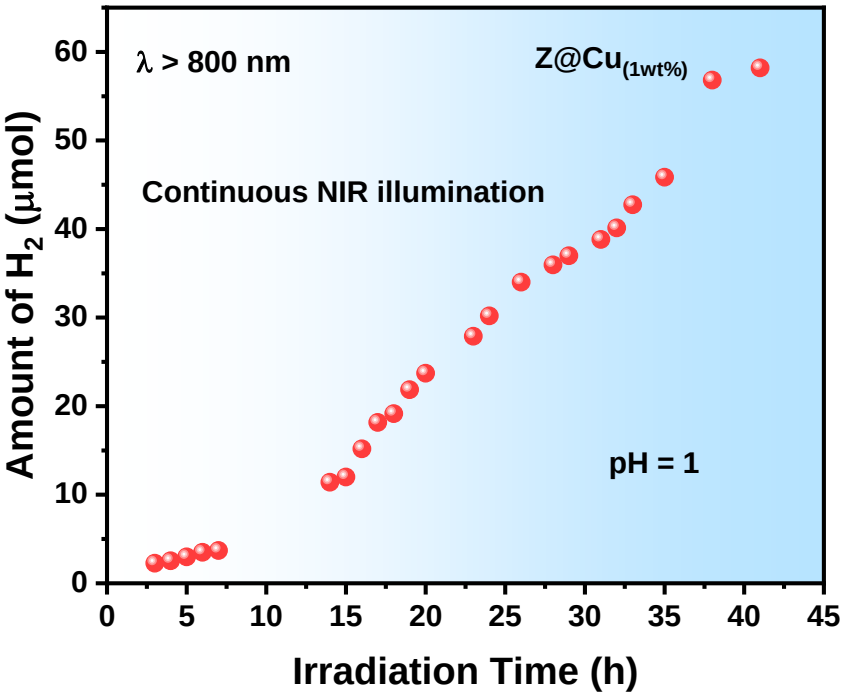

Fig. S9. Photostability evaluations under acidic medium (pH = 1).

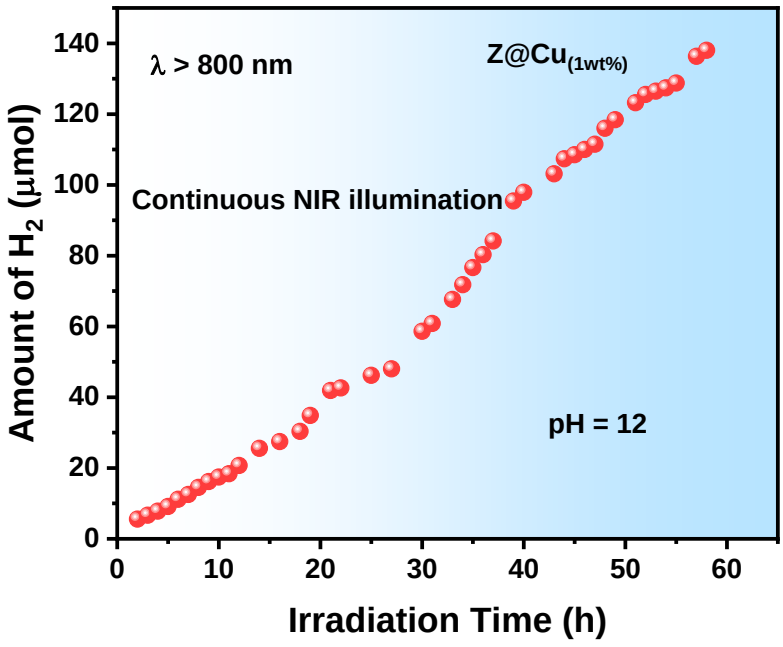

Fig. S10. Photostability evaluations under alkaline medium (pH = 12).

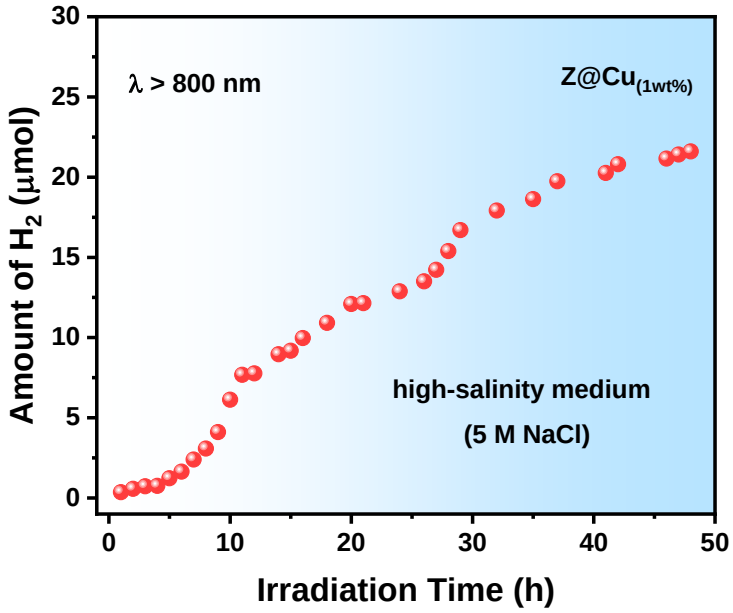

Fig. S11. H_2 production performance in highly saline medium (5 M NaCl) under NIR light irradiation.

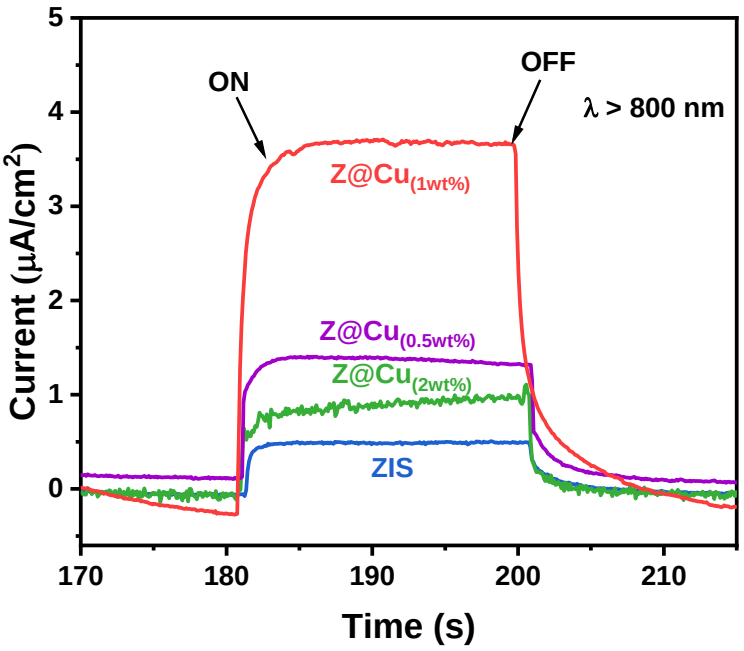

Fig. S12. Periodic on/off photocurrent responses of as-obtained sample under NIR light irradiation (λ > 800 nm).

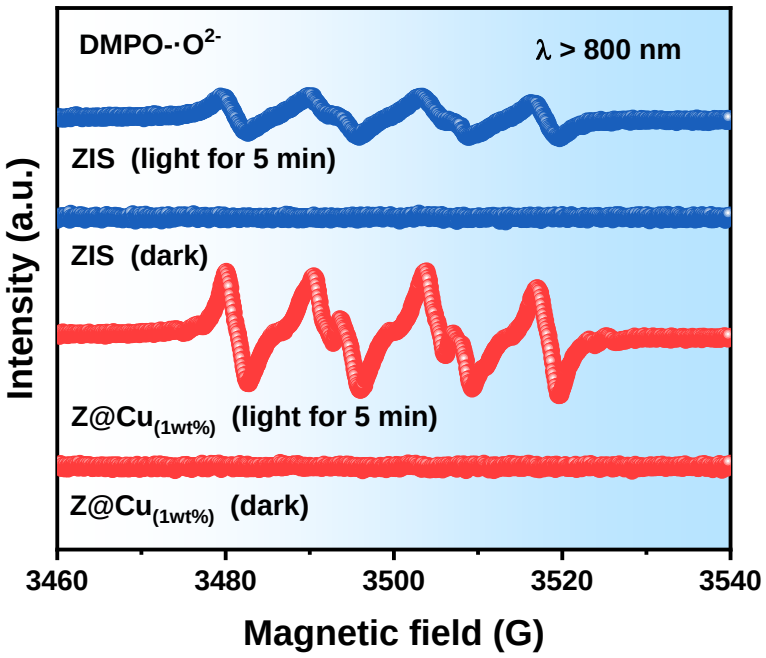

Fig. S13. EPR spectra of DMPO-O^{2-}radicals for the as-prepared samples under NIR light irradiation (λ > 800 nm).

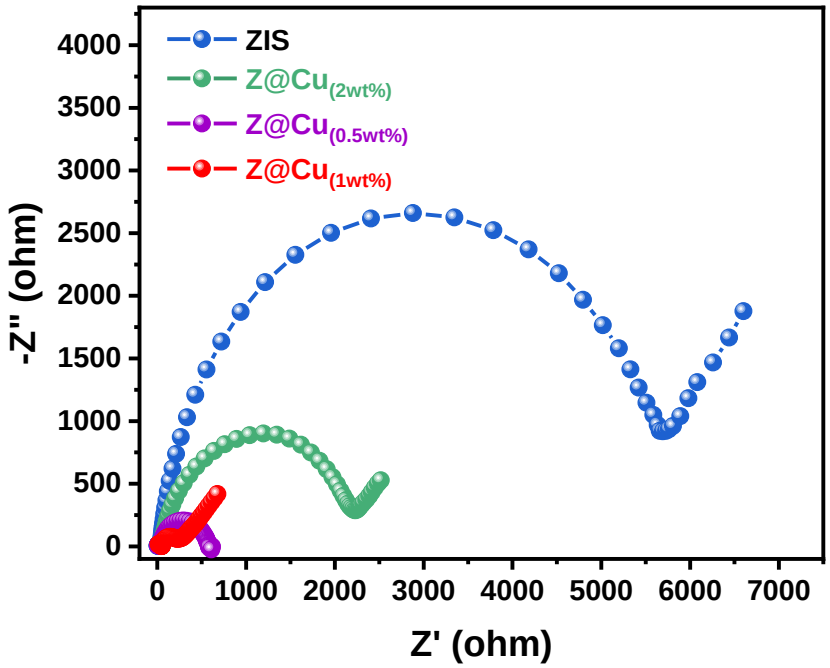

Fig. S14. EIS Nyquist plots of $ZnIn_2S_4$ with varied CuSe loading contents.

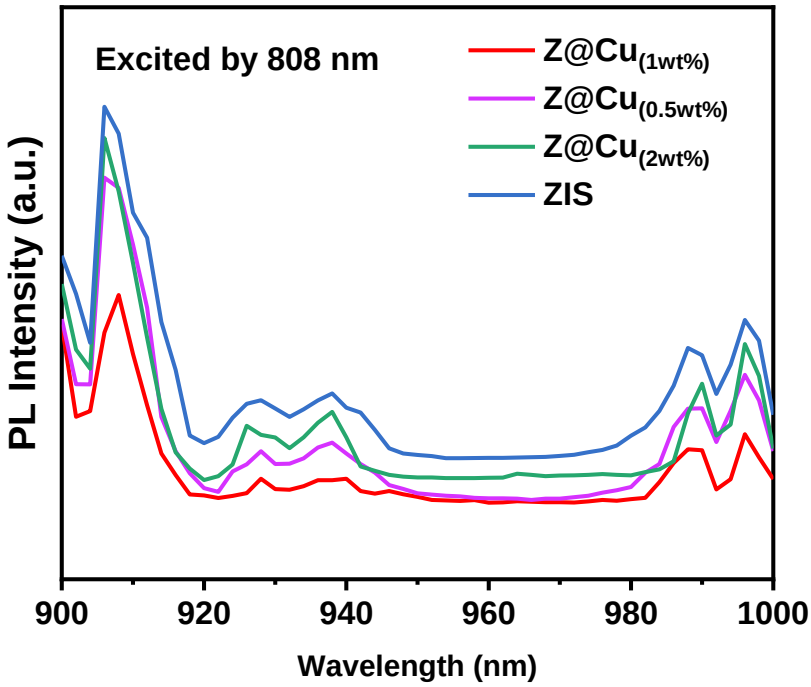

Fig. S15. Steady-state PL spectra at 298 K under 808 nm excitation.

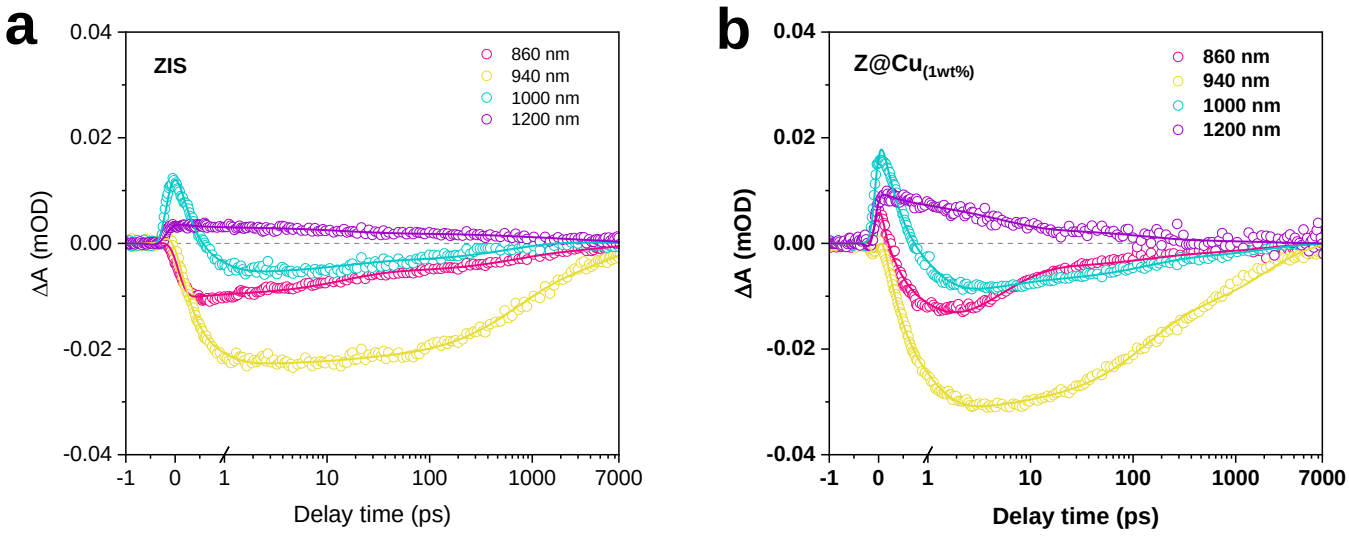

Fig. S16. Comparative relaxation dynamics of the ZIS and Z@Cu$_{(1wt\%)}$ probed at 860, 940, 1000, and 1200 nm.

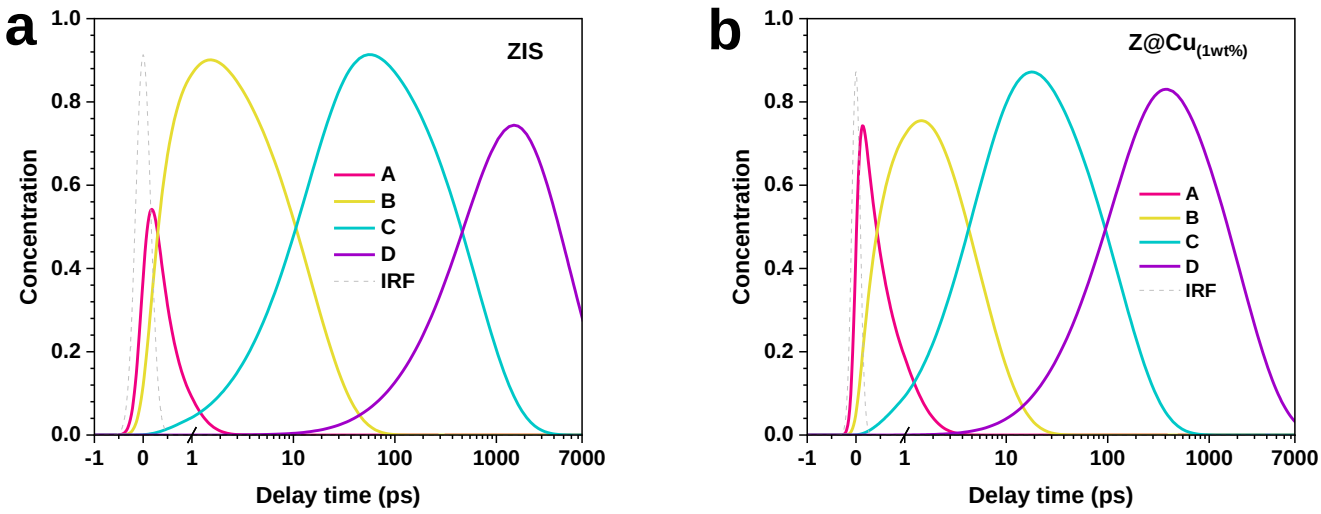

Fig. S17. Temporal evolution of species concentrations, with the leftmost feature representing the fitted instrument response function (IRF).

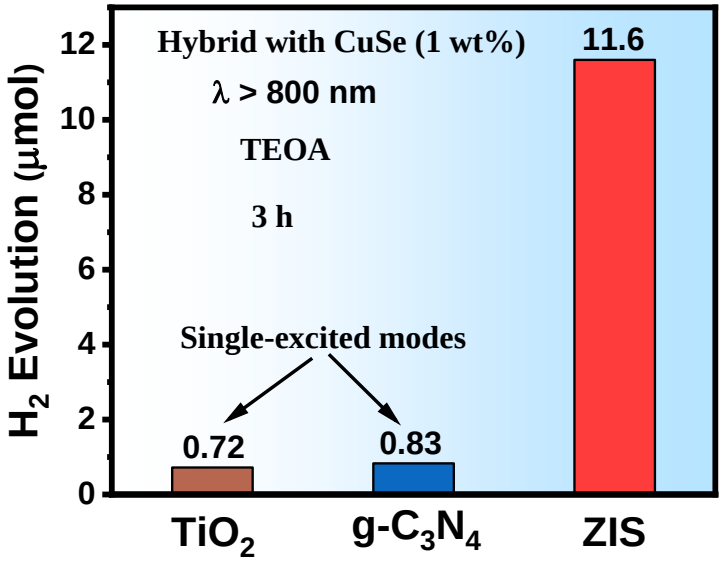

Fig. S18. The comparison of H_2 production performance on PMDE and PMSE modes under NIR light irradiation.

Table S1. Summary of currently reported NIR-responsive plasmonic photocatalytic systems and their performance in the water splitting half-reaction for H_2 production under identical conditions.

	NIR-responsive photocatalysts	Extended Wavelength (nm)	Sacrificial Agents	H_2 production (μmol/h)	Ref.
Adding noble metals	Pt@$Cu_{7.2}S_4$/g-C_3N_4	λ > 800 nm	triethanolamine	1.64	*Int. J. Hydrogen Energy* **2023**, 48(63), 24285–24294
	Pt@CuS/CdS	λ > 800 nm	methanol	0.48	*Nat. Sustain.* **2022**, 5, 1092–1099
	Pt@CuS/ZnS	λ > 800 nm	Na_2S/Na_2SO_3	0.1345	*J. Am. Chem. Soc.* **2023**, 145(28), 15482–15487
	Pt@Cu_7S_4/CdS	λ > 800 nm	Na_2S/Na_2SO_3	0.147	*J. AM. Chem. Soc.* **2019**, 141(6), 2446–2450
	Pt@Cu_9S_5/CdS	λ > 800 nm	Na_2S/Na_2SO_3	0.0135	*Appl. Catal. B-Environ.* **2022**, 318, 121860
	Pt@$SnFe_2O_4$@$ZnIn_2S_4$	λ > 800 nm	triethanolamine	0.4475	*Chinese Chem. Lett.* **2025**, 36, 111302
Without adding noble metals	$Cs_{0.33}WO_3$/CdS	λ > 800 nm	Na_2S/Na_2SO_3	0.8	*Appl. Surf. Sci.* **2020**, 508, 145200
	$W_{18}O_{49}$/$Cd_{0.5}Zn_{0.5}S$	λ > 800 nm	Na_2S/Na_2SO_3	3.5	*Chinese J. Catal.* **2022**, 43(2), 234–245
	CuSe/$ZnIn_2S_4$	λ > 800 nm	triethanolamine	3.87	**This work**

Table S2. Comparison of previously reported NIR-activated hybrid photocatalysts beyond 900 nm for photocatalytic H_2 production activity to date (N.A.: not available).

	Photocatalysts	Wavelength (nm)	H_2 production (μmol/h)	AQY	Ref.
Without adding noble metals	Z@$Cu_{(1wt\%)}$	λ = 940 nm	2.18	3.0%	**This work**
	PA-Ni@$PCN_{(1:1)}$	λ = 940 nm	0.44	2.8%	*Angew. Chem. Int. Edit.* **2021**, 60(10), 5245–5249
	WO_2−Na_xWO_3	λ = 980 nm	0.015	N.A.	*Nano Lett.* **2015**, 15, 7199–7203.
Adding noble metals	(UCNPs)-Pt@MOF/Au	λ = 980 nm	0.34	N.A.	*Adv. Mater.* **2018**, 30, 1707377.
	Pt@Cu_7S_4/CdS	λ = 1100 nm	N.A.	3.8%	*J. AM. Chem. Soc.* **2019**, 141(6), 2446–2450
	Pt@CuS/CdS	λ = 1100 nm	N.A.	0.6%	*Nat. Sustain.* **2022**, 5, 1092–1099
	Pt@CuS/ZnS	λ = 1100 nm	N.A.	1.07%	*J. Am. Chem. Soc.* **2023**, 145(28), 15482–15487
	Pt@Cu_9S_5/CdS	λ = 1100 nm	N.A.	4.4%	*Appl. Catal. B-Environ.* **2022**, 318, 121860
	Au@Cu_7S_4	λ = 2200 nm	N.A.	7.3%	*Nat. Commun.* **2024**, 15, 413
	Au nanorods/$La_2Ti_2O_7$	λ = 920 nm	N.A.	1.2%	*ACS Catal.* **2018**, 8, 122–131

Table S3. Summary of the photostability of previously reported NIR-responsive photocatalytic systems (N.A.: not available) under NIR light irradiation.

	NIR-responsive photocatalysts	Extended Wavelength (nm)	Sacrificial Agents	photostability （h）	Ref.
Adding noble metals	$Pt@Cu_7S_4/CdS$	$\lambda > 800$ nm	Na_2S/Na_2SO_3	35	*J. AM. Chem. Soc.* **2019**, 141(6), 2446–2450
	Pt@CuS/CdS	$\lambda > 800$ nm	methanol	172	*Nat. Sustain.* **2022**, 5, 1092–1099
	$BP/Au/La_2TiO_7$	$\lambda > 780$ nm	methanol	12	*Angew. Chem. Int. Edit.* **2017**, 56(8), 2064–2068
	$Au@Cu_7S_4$	N.A.	methanol and glucose	30	*Nat. Commun.* **2024**, 15, 413
	S-doped $g\text{-}C_3N_4$@Pt	$\lambda > 800$ nm	triethanolamine	24	*Appl. Catal. B-Environ.* **2023**, 325, 122292
	$Pt@Cu_{7.2}S_4/g\text{-}C_3N_4$	$\lambda > 800$ nm	triethanolamine	20	*Int. J. Hydrogen Energy* **2023**, 48(63), 24285–24294
	$Pt@Cu_9S_5/CdS$	$\lambda > 800$ nm	Na_2S/Na_2SO_3	42	*Appl. Catal. B-Environ.* **2022**, 318, 121860
	Pt@BP/RGO	$\lambda > 780$ nm	EDTA	20	*Appl. Catal. B-Environ.* **2017**, 217, 285–292
	Pt@C/K-doped $g\text{-}C_3N_4$	700 nm ≤ λ ≤ 780 nm	triethanolamine	2	*Adv. Mater.* **2021**, 33(39), 2101455
	Pt@O-doped $g\text{-}C_3N_4$	$\lambda > 700$ nm	triethanolamine	3	*Adv. Funct. Mater.* **2022**, 32(47), 2207375
	Pt@N-doped C ribbons modified $g\text{-}C_3N_4$	$\lambda > 800$ nm	triethanolamine	5	*Chem. Eng. J.* **2020**, 382, 122870
	Pt@C/O-doped $g\text{-}C_3N_4$	700 < λ < 780 nm	triethanolamine	16	*Adv. Funct. Mater.* **2023**, 33(52), 2305935
	Pt@K-doped $g\text{-}C_3N_4$	700 < λ < 780 nm	triethanolamine	5	*Adv. Sci.* **2022**, 9(21), 2201677
	$Pt@In_2TiO_5$	$\lambda > 800$ nm	methanol	24	*ACS Appl. Mater. Interf.* **2015**, 7(37), 20761–20768
	Ag_2O/TiO_2	$\lambda = 850$ nm	methanol	14	*Int. J. Hydrogen Energy* **2014**, 39, 15411–15415
	PtSn@$g\text{-}C_3N_4$	$\lambda = 765$ nm	triethanolamine	18	*Chem. Commun.* **2020**, 56(45), 6054–6057
	Pt@BP/RGO	$\lambda > 780$ nm	EDTA	4	*Appl. Catal. B-Environ.* **2017**, 217, 285–292
	$BP/Au/La_2TiO_7$	$\lambda > 780$ nm	methanol	12	*Angew. Chem. Int. Edit.* **2017**, 56(8), 2064–2068
	$BP/NaYF_4:Yb^{3+}, Tm^{3+}@Ag_3PO_4$	$\lambda = 980$ nm	glycerol water mixture	25	*Chem. Eng. J.* **2019**, 375, 121967
	BP/Au@CdS	$\lambda > 700$ nm	Na_2S/Na_2SO_3	3	*ACS Energy Lett. **2018**, 3(4), 932–939*
	$W_{18}O_{49}/Au@g\text{-}C_3N_4$	$\lambda > 800$ nm	triethanolamine	7.5	*ACS Appl. Mater. Interf.* **2021**, 13(44), 52670–52680

	Pt@WC/NCN	800–2500 nm	ethanol	5	*ACS Appl. Mater. Interf.* **2021**, 13(39), 46598–46607
	Pt@WN/g-C_3N_4	$\lambda \geq 700$ nm	triethanolamine	20	*Catal. Sci. Technol.* **2022**, 12(24), 7369–7378
	Pt@$W_{18}O_{49}$/g-C_3N_4	$\lambda > 700$ nm	triethanolamine	2	*Mater. Today Adv.* **2022**, 15, 100249
	Pt@$NaYF_4$:Yb^{3+}/Tm^{3+} @$ZnIn_2S_4$	$\lambda > 800$ nm	triethanolamine	2	*J. Environ. Chem. Eng.* **2022**, 10(5), 108352
	β-$NaYF_4$:Yb^{3+}/Tm^{3+} @Ag_3PO_4/Ag@g-C_3N_4	$\lambda > 700$ nm	lactic acid	12	*Chem. Eng. J.* **2021**, 421, 129687
	$NaYF_4$:Yb^{3+},Er^{3+} /Au/CdS	$\lambda > 700$ nm	ethanol	N.A.	*J. Mater. Chem. A.* **2017**, 5(21), 10311–10320
	Pt@Zn-tri-PcNc/TiO_2	$\lambda = 800$ nm	EDTA	15	*RSC Adv.* **2013**, 3(34), 14363–14370
	Pt@Zn-tri-PcNc/g-C_3N_4	$\lambda = 700 \pm 10$ nm	ascorbic acid	30	*ACS Catal.* **2014**, 4(1), 162–170
	Pt@Zn-diPcNcTh-2@g-C_3N_4	$\lambda = 700 \pm 10$ nm	ascorbic acid	32	*Chem. Eng. J.* **2019**, 373, 651–659
Adding noble metals	Pt@ZnPc(K^+)/g-C_3N_4	$\lambda = 700$ nm	triethanolamine	30	*J. Power Sources* **2018**, 396, 57–63
	Pt@PA-Ni@$ZnIn_2S_4$	$\lambda > 800$ nm	triethanolamine	2	*Chem. Eng. J.* **2023**, 474, 145611
	Pt@LI-4/g-C_3N_4/Zn-tri-PcNc	$\lambda = 700$ nm	triethanolamine	30	*ACS Catal.* **2015**, 5(2), 504–510
	Pt@Zn-tri-PcNc-TiO_2-AA	$\lambda > 600$ nm	ascorbic acid	35	*J. Power Sources* **2015**, 298, 30–37
	Pt@Zn-TCPP@CdS	$\lambda > 800$ nm	Na_2S/Na_2SO_3	5	*Int. J. Hydrogen Energy* **2022**, 47(27), 13340–13350
	Pt@eosin Y	$\lambda = 730$ nm	triethanolamine	21	*ACS Catal.* **2023**, 13(6), 3723–3734
	Pt@CDs	$\lambda = 800$ nm	formic acid	4	*Aggregate* **2024**, 5(1), e424
	Au nanorods@MoS_2-CdS (AMC)	$\lambda = 700$ nm	Na_2S/Na_2SO_3	4	*Appl. Catal. B-Environ.* **2023**, 325, 122327
	Pt@ZnP-CPDT	N.A.	ascorbic acid	30	*J. Mater. Chem. A* **2023**, 11, 1473–1481
	Pt@Co_2B/g-C_3N_4	$\lambda > 800$ nm	triethanolamine	20	*Fuel* **2023**, 333, 126280
	Pt@black TiO_2	N.A.	methanol	N.A.	*Science* **2011**, 331, 746

Adding noble metals	Pt@CuS/ZnS	λ > 800 nm	Na_2S/Na_2SO_3	35	*J. Am. Chem. Soc.* ***2023****, 145(28), 15482–15487*
	Pt@glucan aggregates	λ = 630 nm	formic acid	100	*Adv. Mater.* **2026**, 38(5), e15351
	Pt@PITIC-ThF Pdots	λ > 780 nm	ascorbic acid	4	*Nat. Commun.* **2024**, 15, 707
Without adding noble metals	$W_{18}O_{49}/Cd_{0.5}Zn_{0.5}S$	λ > 800 nm	Na_2S/Na_2SO_3	16	*Appl. Surf. Sci.* **2020**, 508, 145200
	$Cs_{0.33}WO_3/CdS$	λ > 800 nm	Na_2S/Na_2SO_3	2	*Chinese J. Catal.* **2022**, 43(2), 234–245
	BP/WS_2	λ > 780 nm	EDTA	12	*Appl. Catal. B-Environ.* **2018**, 221, 645–651
	BP/TiO_2	λ > 780 nm	methanol	Nearly 6	*ACS Catal.* **2019**, 9(4), 3618–3626
	$BP/g\text{-}C_3N_4$	λ > 780 nm	methanol	3	*J. AM. Chem. Soc.* **2017**, 139(37), 13234–13242
	$ZrC/ZnIn_2S_4$	λ > 800 nm	triethanolamine	Nearly 6	*Chem. Eng. J.* **2023**, 474, 145690
	$ZnIn_2S_4$	λ > 800 nm	triethanolamine	20	*Sci. China. Mater.* **2024**, 67(6), 1812–1819
	$FeSi_2$	λ = 950±25 nm	$Na_2S_2O_6$	40	*Chem. Commun.* **2015**, 51(14), 2718–12820
	$Ni_3(C_3N_3S_3)_2$	λ > 760 nm	triethanolamine	24	*Appl. Catal. B-Environ.* **2017**, 210, 205–211
	C_{ring}-doped $g\text{-}C_3N_4$	λ ≥ 800 nm	α-cellulose	N.A.	*ACS Catal.* **2023**, 13(20), 13768–13776
	C-doped $g\text{-}C_3N_4$	700 nm ≤ λ ≤ 780 nm	triethanolamine	4	*Chinese Chem. Lett.* **2021**, 32(11), 3463–3468
	$a\text{-}TiO_{2-x}$	λ > 750 nm	methanol	25	*Green Chem.* **2016**, 18(7), 2056–2062
	$BP/ZnFe_2O_4$	λ > 760 nm	methanol	14	*J. Colloid Interf. Sci.* **2021**, 600, 463–472
	BP/WN	λ > 700 nm	deionized water	5	*Appl. Catal. B-Environ.* **2020**, 267, 118611
	BP QDs/S-HC_3N_4	λ > 800 nm	triethanolamine	20	*Chem. Eng. J.* **2022**, 431, 133453
	BP/MoO_{3-x}	λ > 700 nm	deionized water	25	*ACS Sustainable Chem. Eng.* **2022**, 10(2), 1008–1019
	$BP/CdS@La_2Ti_2O_7$	λ > 700 nm	Na_2S/Na_2SO_3	15	*Appl. Catal. B-Environ.* **2019**, 242, 441–448
	WO_2/Na_xWO_3	λ = 980 nm	phosphate buffer	16	*Nano Lett.* **2015**, 15(11), 7199–7203
	$W_{18}O_{49}/ZnIn_2S_4$	λ > 700 nm	lactic acid	3	*Adv. Funct. Mater.* **2022**, 32(35), 2203638
	WS_2/Cu	λ > 750 nm	lactic acid	30	*Adv. Funct. Mater.* **2018**, 28(43), 1804055
	$W_{18}O_{49}/Cd_{0.5}Zn_{0.5}S$	λ > 800 nm	Na_2S/Na_2SO_3	2	*Chinese J. Catal.* **2022**, 43(2), 234–245
	WN/Bi	λ > 700 nm	deionized water	20	*ACS Appl. Mater. Interf.* **2021**, 13(17), 19884–19893
	β-$NaYF^4$:Yb^{3+}, Tm^{3+}, $Er^{3+}@Cd_{0.5}Zn_{0.5}S$	λ > 800 nm	Na_2S/Na_2SO_3	12	*Int. J. Hydrogen Energy* **2019**, 44(45), 24559–24571
	PA-Ni@ZIS_{1-x}	λ > 800 nm	triethanolamine	20	*Chem. Commun.* **2024**, 60(8), 1035–1038
	$WO_{3-x}/ZnIn_2S_4$	λ > 800 nm	triethanolamine	2	*J. Colloid Interf. Sci.* **2024**, 661, 12–22
	CdZnS/CoP/CoO	λ = 720 nm	lactic acid	7	*Fuel* **2023**, 333, 126331
	$TiO_y@Ti_3C_2/CdS/Cu_2O$	λ > 960 nm	lactic acid	6	*ACS Appl. Mater. Interfaces* **2024**, 16(2), 2204–2215
	$Ti_3C_2T_x$ MXene/CdS	N.A.	Na_2S/Na_2SO_3	20	*J. Mater. Sci. Technol.* **2024**, 171, 1–9

Without adding noble metals	$Cu_{1.8}S$@CdS	$\lambda \geq 780$ nm	Na_2S/Na_2SO_3	16	*Sep. Purif. Tecnol.* **2025**, 353, 128305
	$CdS/Bi/Bi_2WO_6/Bi_2S_3$	$\lambda = 700$ nm	lactic acid	20	*J. Mater. Chem. A* **2024**, 2, 18498–18511
	PA-Ni@g-C_3N_4	$\lambda > 800$ nm	methanol	20	*Angew. Chem. Int. Edit.* **2021**, 60, 5245–5249
	$CuCrP_2S_6$	$\lambda > 780$ nm	triethanolamine	16	*Adv. Mater.* **2024**, 36(32), 2404833
	TCPP	$\lambda = 850 \pm 10$ nm	N.A.	24	*Nat. Energy* **2023**, 8, 361–371
	CuSe/$ZnIn_2S_4$	$\lambda > 800$ nm	triethanolamine	over 48	**This work**

References

1 Y. Y. Huang, H. Yang, S. Feng, C. W. Ma, P. Y. Cao, F. F. Li, X. Y. Lu, W. D. Shi, *Sci. China Mater.* 2024, **67**, 1812–1819.

2 G. Kresse, J. Furthmüller, *Phys. Rev. B* 1996, **54**, 11169–11186.

3 J. P. Perdew, K. Burke, M. Ernzerhof, *Phys. Rev. Lett.* 1996, **77**, 3865–3868.

4 S. Grimme, J. Antony, S. Ehrlich, H. Krieg, *J. Chem. Phys.* 2010, **132**, 154104.

5 E. Sanville, S. D. Kenny, R. Smith, G. Henkelman, *J. Comp. Chem.* 2007, **28(5)**, 899–908.

6 P. E. Blöchl. *Physi. Rev. B* 1994, **50(24)**, 17953.